Manuscript

Self-gating in semiconductor electrocatalysis

Yongmin He[1,2†], Qiyuan He[1†], Luqing Wang[3], Chao Zhu[1], Prafful Golani[1], Albertus D. Handoko[4], Xuechao Yu[2], Caitian Gao[2], Mengning Ding[5], Xuewen Wang[1], Fucai Liu[6], Qingsheng Zeng[1], Peng Yu[1], Shasha Guo[1], Boris Yakobson[3], Liang Wang[7], Zhi Wei Seh[4], Zhuhua Zhang[8], Minghong Wu[7], Qi Jie Wang[2, 9*], Hua Zhang[1,10]*, and Zheng Liu[1,9,11,12]*

[1]School of Materials Science and Engineering, Nanyang Technological University, Singapore 639798, Singapore.
[2]Center for OptoElectronics and Biophotonics, School of Electrical and Electronic Engineering & The Photonics Institute, Nanyang Technological University, Singapore 639798, Singapore.
[3]Department of Materials Science and NanoEngineering, Rice University, Houston, Texas 77005, United States.
[4]Institute of Materials Research and Engineering, Agency for Science, Technology and Research (A*STAR), 2 Fusionopolis Way, Innovis, Singapore 138634, Singapore.
[5]Key Laboratory of Mesoscopic Chemistry of MOE, School of Chemistry and Chemical Engineering, Nanjing University, Nanjing 210023, China.
[6]School of Optoelectronic Science and Engineering, University of Electronic Science and Technology of China, Chengdu 610054, China.
[7]School of Environmental and Chemical Engineering, Shanghai University, Shanghai 200444, P.R. China.
[8]State Key Laboratory of Mechanics and Control of Mechanical Structures, and Institute of Nanoscience, Nanjing University of Aeronautics and Astronautics, Nanjing 210016, China.
[9]CINTRA CNRS/NTU/THALES, UMI 3288, Research Techno Plaza, Singapore, Singapore.
[10]Department of Chemistry, City University of Hong Kong, Kowloon, Hong Kong, China.
[11]School of Electrical and Electronic Engineering, Nanyang Technological University, Singapore, Singapore
[12]Environmental Chemistry and Materials Centre, Nanyang Environment and Water Research Institute, Singapore, Singapore.
[†]Yongmin He and Qiyuan He contributed equally to this work.

[*]E-mail: z.liu@ntu.edu.sg, HZhang@ntu.edu.sg, hua.zhang@cityu.edu.hk, and qjwang@ntu.edu.sg

Abstract:

The semiconductor-electrolyte interface dominates the behaviors of semiconductor electrocatalysis, which has been modeled as a Schottky-analog junction according to the classic electron transfer theories. However, this model cannot be used to explain the extremely high carrier accumulations in ultrathin semiconductor catalysis observed in our work. Inspired by the recently developed ion-controlled electronics, we revisited the semiconductor-electrolyte interface and unraveled a universal self-gating phenomenon through micro-cell based *in-situ* electronic/electrochemical measurements to clarify the electronic-conduction modulation of semiconductors during electrocatalytic reaction. Then we demonstrate that the type of semiconductor catalysts strongly correlates their electrocatalysis, *i.e.*, *n*-type semiconductor catalysts favor cathodic reactions such as hydrogen evolution reaction (HER), *p*-type ones prefer anodic reactions such as oxygen evolution reaction (OER), and bipolar ones tend to perform both anodic and cathodic reactions. Our study provides a new insight into the electronic origin of semiconductor-electrolyte interface during electrocatalysis, paving the way for designing high-performance semiconductor catalysts.

Text:

The semiconductor-electrolyte interface governs the semiconductor electrocatalytic behaviors.[1-4] In fundamental electrochemistry, the Schottky-analog junction is used to model the charge-transfer kinetics across the interface during electrochemical reactions[5-7], according to classic electron transfer theories (*e.g.* Marcus theory[8] and Gerischer Model[9]). In such case, the charge transfer process is determined by the band alignment between the semiconductor and the redox species, and the interface is considered fully active for such process. On the other hand, from an electronics point of view, metal-insulator-semiconductor (MIS) junction is used to describe the semiconductor-electrolyte interface, especially for the charge-transport modulation, in the emerging field of ion-controlled electronics (ionic gating or electrochemical gating) [10-14]. In this case, the interface is considered fully inert without charge transfer process, and thus is capable of accumulating an extremely high surface charge concentration (exceeding 10^{14} e cm^{-2}) through a ultrahigh electric field (in the order of 10 MV cm^{-1}), making semiconductor highly conductive[10,11] or even superconductive[15,16].

Recent works imply that the semiconductor electrocatalytic surface can be considered as a mixture of "active" and "inert" regions, and the charge transfer process mainly occurs at certain active crystal planes in bulk materials[17-19] or at the atomically active sites (*e.g.* defects or edges) in ultrathin materials[20-22]. Unfortunately, such mixed interface cannot be well described by the Schottky-analog junction or MIS junction.

Here, by using the micro-cell based *in-situ* electronic/electrochemical measurements, we found that the electrocatalytic reaction itself can strongly modulate the surface conductance of semiconductor electrocatalysts, defined as *self-gating*. As a result, the surface can be modulated to be high-conductive

("on") or insulating ("off"), strongly correlating the electrocatalytic reactions. The self-gating phenomenon can explain why ultrathin semiconductors can be used as highly efficient electrocatalysts, although semiconductors have been predicted as non-ideal catalysts due to their low intrinsic carrier concentration[23]. Importantly, our experiments suggest that the self-gating phenomena could universally exist in various semiconductors, including two-dimensional (2D) transition metal dichalcogenides (TMDs) and one-dimensional (1D) Si nanowires.

In our experiment, a four-electrode micro-cell (Fig. 1a and S1-S2)[24,25] was used to simultaneously collect the electronic and electrochemical signals of semiconductor electrocatalysts, *i.e.*, the *in-situ* electronic/electrochemical measurement, and ultrathin TMD nanosheets[20,22] are used as semiconductor electrocatalysts. Figure 1b shows the optical image of the fabricated micro-cell, *i.e.*, the overall setup shown in Fig. 1b(i). The micro-electrochemical environment, and the device are shown in Fig. 1b(ii) and (iii), respectively. Spatial control of the electrocatalytic reaction was achieved by carving a small window on a passive poly(methylmethacrylate) (PMMA) layer, ensuring that the reaction only occurs on the region of interest (Fig. S3). The detailed information about the calibration and measurement of micro-cell is shown in Fig. S4-S6.

By using the fabricated micro-cell, we first conducted the *in-situ* electronic/electrochemical measurement on a single-layer WS_2 nanosheet with thickness of 6.5 Å. Figure 1c shows its electrochemical (polarization curves, black y axis) and the electronic (conductance curves, red y axis) measurements during the hydrogen evolution reaction (HER) at various drain-source voltages (V_{ds}: 0 to 50 mV). In the electrochemical measurement, its HER performance (onset potential of ≈ -208 mV *vs*. RHE and Tafel slope of ≈ 108 mV dec^{-1}, see Supplementary Fig. S7) is comparable with the

previously reported single-layer WS_2[22,26]. In the electronic measurement, the drain-source current (I_{ds}) shows an on/off ratio of 10^4 (V_{ds} = 50 mV) and a very small saturation potential (≈ -0.4 V *vs*. RHE), indicating an efficient conductance modulation of single-layer WS_2 during HER. These electronic transport results closely resemble a typical ionic-gating transistor[11,27] with an *n*-type semiconducting characteristics, which was proved by back-gated measurement on the same device (inset in Fig. 1c). In a classic field-effect transistor (FET), the conductance modulation is realized through the gate electrode.[11,27,28] However, in our experiment, the conductance modulation relies on the electrochemical potential itself without any additional gate electrode. Therefore, we define this phenomenon as self-gating. The gating strength is expressed by $\Delta V_G = \Delta E_f/e + \Delta\phi$[29,30], where ΔV_G is the change of the gate voltage (*i.e.*, the inverse value of the electrochemical potential), ΔE_f is the change of chemical potential (Fermi level), *e* is the elementary charge, and $\Delta\phi$ is the change of electrostatic potential. In an aqueous electrolyte (0.5 M H_2SO_4), $e\Delta V_G \cong \Delta E_f$ is obtained (see detailed calculation in Supplementary Note 1), suggesting an effective tuning of the semiconductor's Fermi level during electrocatalysis.

Importantly, the self-gating phenomenon is valid for various ultrathin semiconductor catalysts. Figures 1d-f show the electronic signals (upper panels, red curves) and the electrochemical signals (lower panel, green curves) of three types of semiconducting TMDs with different majority charge carriers (electrons, holes, and both). In the electronic measurements, MoS_2, as an *n*-type semiconductor, shows a threshold voltage of -50 mV (*vs*. RHE) and on/off ratio of 5×10^3 (Fig. 1d). As a *p*-type semiconductor, $WSe_{1.8}Te_{0.2}$ shows a threshold voltage of 960 mV (*vs*. RHE) and on/off ratio over 10^4 (Fig. 1e). Clearly, the bipolar WSe_2 shows two threshold voltages at both polarity (Fig. 1f). Their back-gated measurements on the same devices further proved their semiconducting characteristics (*n*-type

for MoS_2, *p*-type for $WSe_{1.8}Te_{0.2}$, and bipolar for WSe_2), as shown in Fig. S8. Interestingly, in our experiment, the bandgap of bipolar WSe_2 (≈ 1.13 eV, see Supplementary Note 2) can be directly extracted from the electronic characteristics in Fig. 1f, which aligns well with the reported values (1.10 to 1.30 eV)[28], experimentally confirming the effective tuning of Fermi level ($e\Delta V_G \cong \Delta E_f$), *i.e.*, self-gating. This is also confirmed by the observed low subthreshold swing, *i.e.*, 68 mV/dec (Fig. S9), which is close to the ideal value (60 mV dec^{-1} at room temperature) in electronic measurement[30,31]. Moreover, we also observed such kind of gating phenomenon in other semiconducting TMD catalysts, such as ReS_2 (Fig. S10), $PtSe_2$ (Fig. S11), and $MoTe_2$ (Fig. S12) and in different electrolyte conditions, such as salt and buffer solutions (Fig. S13).

The lower panels of Fig. 1d-f show the electrochemical measurements of *n*-type MoS_2, *p*-type $WSe_{1.8}Te_{0.2}$, and bipolar WSe_2, and their corresponding Tafel plots are shown in Fig. S14. The *n*-type MoS_2 is turned on by self-gating at negative potential of -0.05 V (*vs*. RHE), and delivers a high conductance, for example, 2.60 Ω mm at -0.19 V (*vs*. RHE) and 0.61 Ω mm at -0.48 V (*vs*. RHE), thus showing HER activity (Fig. 1d and S14a). At positive potential, MoS_2 is turned off with a low conductance (≈ 2975.6 Ω mm), showing no electrochemical activity. As comparison, *p*-type $WSe_{1.8}Te_{0.2}$ is turned on at positive potential of 0.96 V (*vs*. RHE), while turned off at the negative potential, only exhibiting OER activity (Fig. 1e and S14b). Furthermore, bipolar WSe_2 can be turned on at both negative (-0.28 V *vs*. RHE) and positive (0.85 V *vs*. RHE) potentials, performing both HER and OER activities (Fig. 1f and S14c-d). These results suggest the electrochemical reactions can only occur when the ultrathin semiconductor catalysts are turned on by self-gating. Otherwise, they behave like an insulator without any electrochemical reactions when they are turned off by self-gating. Under self-gating, the strong correlation between the semiconducting types and the suitable catalytic reactions

can be applied to other semiconducting TMD catalysts, such as ReS_2, $PtSe_2$, and $MoTe_2$ (Fig. S10-12).

From a fundamental electrochemistry point of view, we measured the electrochemical impedance spectroscopy (EIS) in our micro-cell (Fig. 1a and S15) to identify self-gating on MoS_2 during HER. As a control experiment, Au was tested (Fig. S16). It showed a comparable HER performance with MoS_2 (Fig. S17), representing a metal-electrolyte interface. The Nyquist plots of Au and MoS_2 nanosheet microelectrodes at various electrochemical potentials in HER are shown in Fig. 2a and 2d, respectively. Their corresponding bode angle (θ-f) plots are shown in Fig. 2b and Fig. 2e, respectively. The EIS data for Au electrode can fit to an equivalent circuit containing a parallel R_{ctr}/Q_{edl} elements (Fig. 2c), which can be interpreted as Faradic charge transfer process. Interestingly, the EIS data obtained from the MoS_2 nanosheet can fit into two series of equivalent circuits (Fig. 2f). The low-frequency element is similar to Au (Fig. 2c), while the high-frequency one can be fit into a parallel *R/C* equivalent circuit (blue circuit in Fig. 2f), indicating charge transport to the electrocatalytic interface. This step could be associated with the charge transport resistance (R_{ctt}), and quantum capacitance (C_q) for ultrathin MoS_2 nanosheet[32-34]. Both R_{ctt} and C_q exhibit strong electrochemical potential dependence, as shown in Fig. 2g and Fig. 2h, respectively. R_{ctt} increases with the electrochemical potential, which aligns well with the self-gating induced conductance decrease in MoS_2 nanosheet, which is an *n*-type semiconductor (Fig 1d). Notably, R_{ctt} directly extracted from the EIS (green in Fig. 2g) is comparable to the resistance (*R*) obtained from *in-situ* electronic measurement (red in Fig. 2g and S17b), indicating that our *in-situ* electronic/electrochemical measurement is valid. C_q increases with negative electrochemical potential (Fig. 2h), indicating that the Fermi level is tuned deeper inside the conduction band of MoS_2 by self-gating, similar to the observations in top-gated FETs.[32,33] In addition, there is no obvious change of total capacitance (C_{total}, series-connected

capacitors of C_q and C_{edl}) across the whole semiconductor-electrolyte interface in the electrochemical potential range (Fig. 2i), suggesting a quasi-stable self-gating during the electrocatalytic reaction.

The observed self-gating phenomenon is distinct from the classic electron transfer theories. Current electron transfer theories[1-4], including Marcus theory and the Gerischer Model, assume a fully active semiconductor-electrolyte interface that works as a Schottky-analog junction, in which the majority carriers can be accumulated under the electrochemical potential. However, similar to the junction field-effect transistors[35,36], it is difficult for such junction to accumulate a high carrier concentration or achieve a high conductivity *i.e.*, the Fermi level deep inside the conduction or valence band, because the Schottky-analog junction approaches Ohmic characteristic once the charge transfer process, *i.e.*, the electrochemical reaction starts. On the other hand, the recently developed ion-controlled electronics assume a fully inert interface, which works as a ionic gating or metal-insulator-semiconductor (MIS) junction[28,37]. Such ionic gating is capable of accumulating an extremely high charge concentration (exceeding 10^{14} e cm^{-2} in 2D semiconductors) to make semiconductor conductive[10,11] or even superconductive[15,16]. However, since the current electron transfer theories mainly focus on the active region while overlook the inert region, they cannot be used to explain the exceptionally high carrier accumulation observed in our experiment. Based on our experiments on different types of semiconductors, we propose that, in terms of the carrier modulation, a practical semiconductor-electrolyte interface containing both active and inert regions can be modeled as a leakage metal-insulator-semiconductor (LMIS) junction, *i.e.*, leakage ionic gating, see Supplementary Table S3, and Fig. S18-S20 for details. In this model, the *leakage* refers to the charge transfer process from the active region to reactant, and the *MIS* refers to the self-gating modulated surface conductance, which will be further discussed below.

The middle panel of Fig. 3a schematically illustrates a device of a 35-nm-thick MoS_2 flake with top and bottom electrodes (see device fabrication in Fig. S21), where both surface and bulk conductance can be measured during HER. A strong self-gating phenomenon is observed on the top-electrode device (left panel in Fig. 3a). However, a weak conductance modulation is observed on the bottom-electrode device (right panel in Fig. 3a). That is, a high surface conductance is only observed at the top surface of MoS_2, resulting in the higher HER activity, compared to the bulk of MoS_2 with low conductance.

Then we examined the penetration depth of surface conductance in the device with a bottom electrode configuration (inset of Fig. 3b and S22), where the electrochemical current transports vertically through the MoS_2 flake to the bottom electrode. Figures 3b shows the MoS_2-thicknesses-dependent HER current density at -0.4 V *vs*. RHE (see polarization curves in Fig S23b). Obviously, 1 nm single-layer MoS_2 (see the first image in Fig. S22) shows the highest HER activity ($j_{max} \approx 150$ mA cm^{-2}). The current decays rapidly with the MoS_2 thickness ($j/j_{max} = 50\%$ and 10% at 5 and 16 nm MoS_2, respectively). When the MoS_2 thickness exceeds 40 nm, it does not show obvious HER activity. Here, we define the penetration depth at 1% of the max current (*e.g.* $j/j_{max} = 1\%$), which is ≈ 25 nm for MoS_2 in HER. From the aspect of semiconducting electronics, the penetration depth of surface conductance is determined by the carrier density at the accumulation regime under self-gating. Our theoretical calculation (see Supplementary Note 4 and Fig. S24) shows that such depth is estimated to be about tens of nanometers beneath the semiconductor surface (Fig. 3c), in line with our experimental results.

To the best of our knowledge, the aforementioned surface conductance has not been investigated in semiconductor electrocatalysis. In our experiment, we found that self-gating could induce a charge

transport pathway which renders the surface of semiconductors highly conductive (Fig. 3d). As a result, charge carriers can transport within the surface of semiconductor instead of its bulk, which is different from the metallic electrocatalyst that charge carriers transport through its high conductive bulk (see detailed discussion in Supplementary Note 5). Importantly, the concept of surface conductance can explain the high electrocatalytic activities of nanostructured semiconductor catalysts, such as metal oxide[38-41] and 2D metal dichalcogenides[20,22,42], because they can be effectively modulated into high-conductive state once their thickness is within the accumulation regime. It can also explain the high activities of previously reported semiconductor catalysts even without conductive additives[22,43,44]. Therefore, the surface conductance strongly correlates the electrocatalytic activity of a semiconductor catalyst.

As shown in Fig. 4a, when the semiconductor catalyst is turned on under self-gating, its surface becomes conductive and the cathodic reaction happens. Otherwise, its surface is insulated without electrocatalytic reactions (Fig. 4b). As a result, *n*-type semiconductor catalysts can be turned on by the negative electrochemical potential (positive gating), making them suited for cathodic reactions, such as HER and CO_2 reduction (Fig. 4c). Alternatively, *p*-type semiconductor catalysts can be turned on by the positive electrochemical potential (negative gating), resulting in anodic reactions, such as OER and oxygen reduction reaction (ORR). As for bipolar semiconductor catalysts, they can be turned on by both positive and negative potentials, leading to anodic and cathodic reactions, respectively. This principle has been proved by our experiments on various materials, including 2D materials, such as WS_2 (Fig 1c), MoS_2 (Fig. 1d and Fig. S17b), WSe_2 (Fig. 1f), ReS_2 (Fig. S10), $PtSe_2$ (Fig. S11), $MoTe_2$ (Fig. S12), and $WSe_{1.8}Te_{0.2}$ (Fig. 1e), and conventional semiconductors, such as *n*-type, *p*-type and bipolar Si nanowires (Fig. S25), and previously reported thin films, such as *p*-type $Co_{1-x}Fe_xOOH$[43]

and $Ni_{1-x}Fe_xOOH$[44]. It is worth mentioning that the efficient charge transport in semiconductors under self-gating is necessary for electrocatalytic reaction to occur. On the other hand, the *intrinsic catalytic activity* of the semiconductor is another important factor that affects the charge transfer kinetics at the electrocatalytic reaction interface[45]. Both of them contribute to the semiconductor electrocatalysis.

Table 1 summarizes the correlation between charge carrier types of the commonly used semiconductors and their preferred electrocatalytic reactions (HER, OER, CO_2 reduction, or ORR). For example, *n*-type MX_2 (M= Mo, W, Re; X = S, Se) catalyst favors the HER, *p*-type Ni and Co based catalysts prefer the OER and ORR, and bipolar Ta/Nb doped MoS_2 (or WS_2) catalysts tend to perform both HER and ORR (see detailed discussions in Supplementary Note 6). Our work provides a clear and comprehensive understanding of semiconductor-electrolyte interface by bridging electrochemical activities with electronic states, and can further guide the rational design of semiconductor catalysts for various promising catalytic applications. Beyond the electrocatalysis, the demonstration of self-gating can improve our understanding on a large variety of semiconductor-electrolyte interfaces in photoelectrochemical catalysis, photocatalysis, supercapacitor, and batteries.

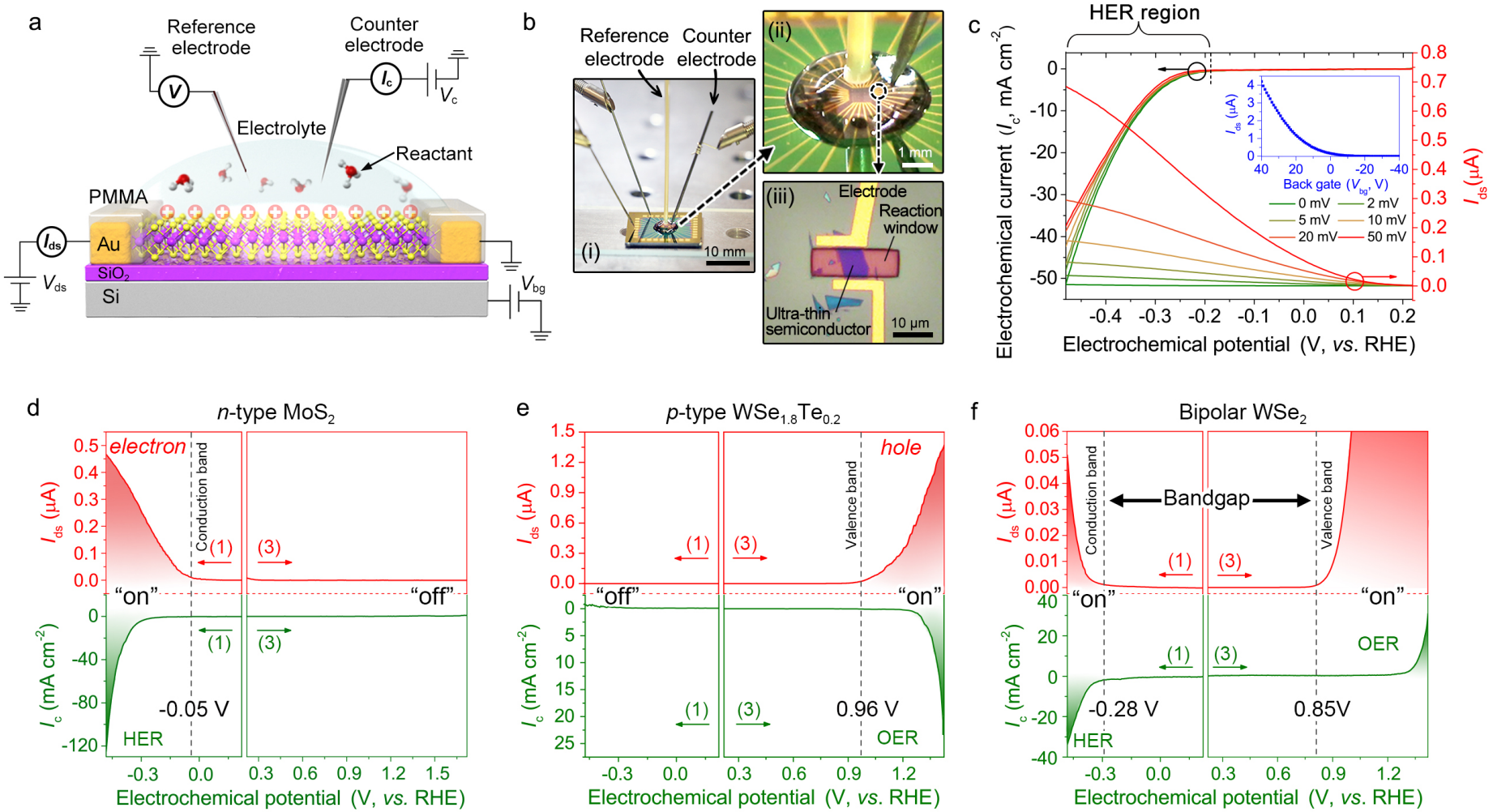

Figure 1. Demonstration of self-gating phenomenon by *in-situ* electronic/electrochemical measurement. a, Schematic illustration of the micro-cell based *in-situ* electronic/electrochemical measurement. Both the electronic signal (I_{ds}, conductance current) and electrochemical signal

(I_c, reaction current) of the transition metal dichalcogenide (TMD) nanosheet can be simultaneously collected. Before the *in-situ* electronic/electrochemical measurement, the type of majority charge carrier for each device is pre-identified by the back-gated measurement (V_{bg}) on SiO_2 (285 nm)/Si substrate. **b,** Optical image of the micro-cell: (i) Overall setup with four electrodes, (ii) the zoom-in electrolyte (0.5 M H_2SO_4) droplet in which the reaction occurs, (iii) the mechanically exfoliated TMD device with a micro-size reaction window in the poly(methylmethacrylate) (PMMA) passivation. **c,** Typical electrochemical (y axis in black) and electronic (y axis in red) signals of single-layer WS_2 during hydrogen evolution reaction (HER) at varied bias potentials (V_{ds}: 0, 2, 5, 10, 20 and 50 mV), showing the self-gating phenomenon. Inset: the back-gated measurement on the same device. Note: I_{ds} is normally 10-1000 times I_c. **d-f,** *In-situ* electronic/electrochemical measurements of three types of semiconductor electrocatalysts including *n*-type MoS_2 (d), *p*-type $WSe_{1.8}Te_{0.2}$ (e), and bipolar WSe_2 (f). The red curves in top panels are obtained from the electronic measurements, and the green curves in bottom panels are obtained from the electrochemical measurements. The arrows indicate the scan directions of the electrochemical potential (see scans 1 and 3 in Fig. S5 for details). Note: since a large bias voltage would compromise the electrochemical potential, the bias voltage in our experiments was kept at 50 mV to collect electronic signals and ensure minimal interference to the electrochemical signals. In (d), *n*-type MoS_2 is turned on at negative electrochemical potential, and only delivers hydrogen evolution reaction (HER). In (e), *p*-type $WSe_{1.8}Te_{0.2}$ is turned on at positive electrochemical potential, and only delivers oxygen evolution reaction (OER). In (f), bipolar WSe_2 is turned on both negative and positive electrochemical potentials, and can deliver HER and OER, respectively. Accordingly, the Fermi level is tuned to the band edges of the conduction band and the valence band, respectively, experimentally identifying the bandgap.

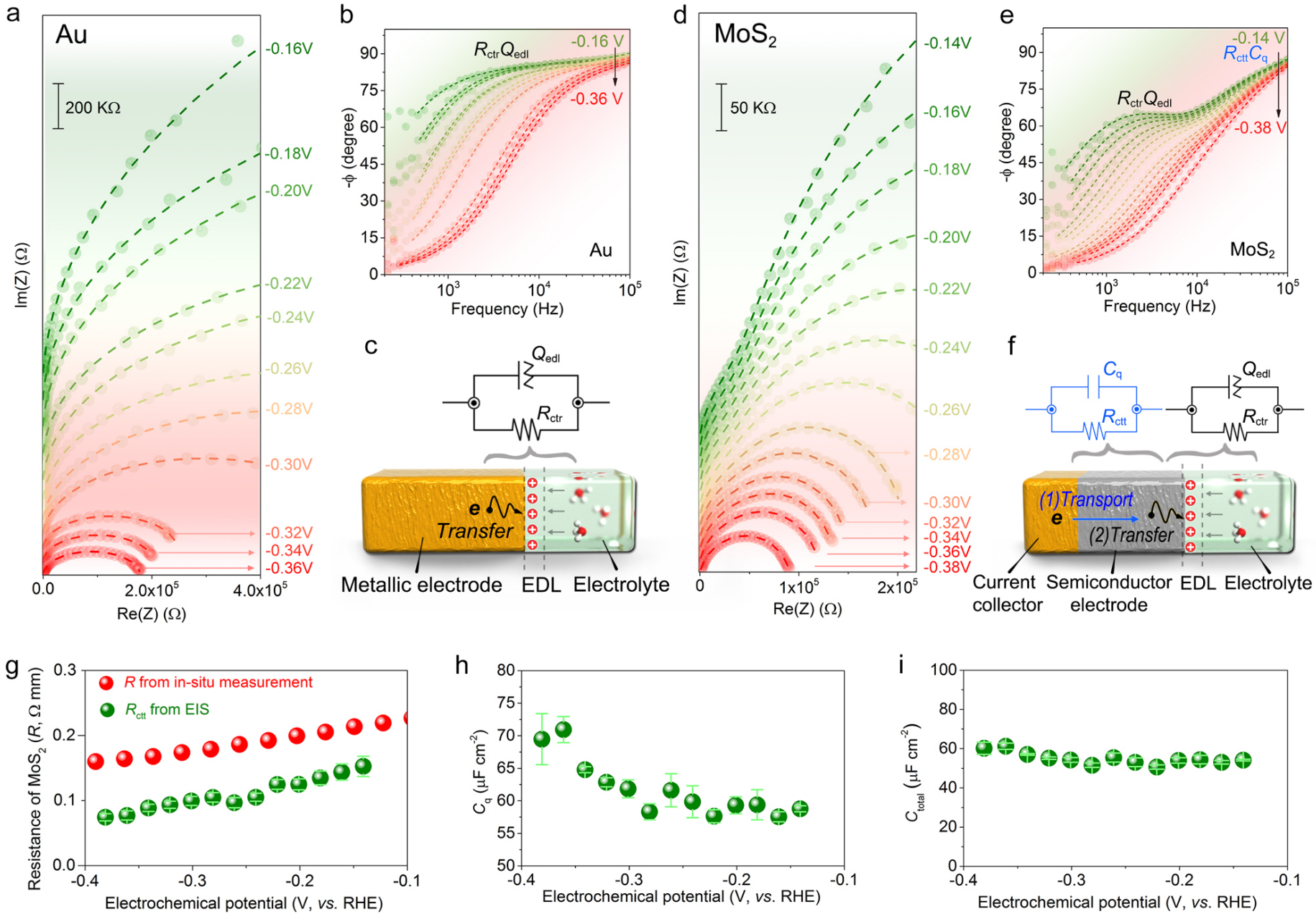
a
Au
200 KΩ
-0.16V
-0.18V
-0.20V
-0.22V
-0.24V
-0.26V
-0.28V
-0.30V
-0.32V
-0.34V
-0.36V
Im(Z) (Ω)
0.0
2.0x10^5
4.0x10^5
Re(Z) (Ω)
b
R_ctr Q_edl
-0.16 V
-0.36 V
-ϕ (degree)
Au
Frequency (Hz)
c
Q_edl
R_ctr
e
Transfer
Metallic electrode
EDL
Electrolyte
d
MoS2
50 KΩ
-0.14V
-0.16V
-0.18V
-0.20V
-0.22V
-0.24V
-0.26V
-0.28V
-0.30V
-0.32V
-0.34V
-0.36V
-0.38V
Im(Z) (Ω)
0
1x10^5
2x10^5
Re(Z) (Ω)
e
-0.14 V
R_ctt C_q
R_ctr Q_edl
-0.38 V
-ϕ (degree)
MoS2
Frequency (Hz)
f
C_q
R_ctt
Q_edl
R_ctr
(1)Transport
e
(2)Transfer
Current collector
Semiconductor electrode
EDL
Electrolyte
g
R from in-situ measurement
R_ctt from EIS
Resistance of MoS2 (R, Ω mm)
Electrochemical potential (V, vs. RHE)
h
C_q (μF cm^-2)
Electrochemical potential (V, vs. RHE)
i
C_total (μF cm^-2)
Electrochemical potential (V, vs. RHE)

Figure 2. Demonstration of self-gating phenomenon by electrochemical impedance spectroscopy (EIS). a-b, Nyquist impedances (a) and bode angles plots (b) of Au microelectrode at various electrochemical potentials (20 mV/step) in HER. **c,** the equivalent Randles circuits (Q_{edl}/R_{ctr}) of the Au microelectrode (see Supplementary Tables S1 and Fig. S15 for details), in which R_{ctr} and Q_{edl} are the charge transfer resistance and the constant-phase element related to the electrical double-layer (EDL) capacitance (C_{edl}), respectively. **d-e,** Nyquist impedances (d) and bode angles plots (e) of the 8-nm-thick MoS_2 nanosheet microelectrode at various electrochemical potentials (20 mV/step) in HER. **f,** the equivalent Randles circuits (Q_q/R_{ctt} +Q_{edl}/R_{ctr}) of the MoS_2 nanosheet microelectrode (See Supplementary Tables S2 and Fig. S16 for details), in which R_{ctt} and C_q are the charge transport resistance and the quantum capacitance, respectively. This Q_q/R_{ctt} circuit shows that the semiconductor electrode undergoes an additional step of charge transport to the electrocatalytic interface, compared to the metallic electrode. All the dashed lines in (a), (b), (d), and (e) are the fitting results according to the respective Randles circuit equivalent. **g,** The consistency of the charge transport resistances of the MoS_2 nanosheet microelectrode measured in both *in-situ* electronic measurement (R, red) and EIS measurement (R_{ctt}, green). **h,** The electrochemical potential-dependent C_q measured in HER. **i,** The total capacitance (C_{total}) of the MoS_2 nanosheet microelectrode calculated based on the equation ($1/C_{total}=1/C_{edl}+1/C_q$), suggesting a quasi-stable self-gating at semiconductor-electrolyte interface.

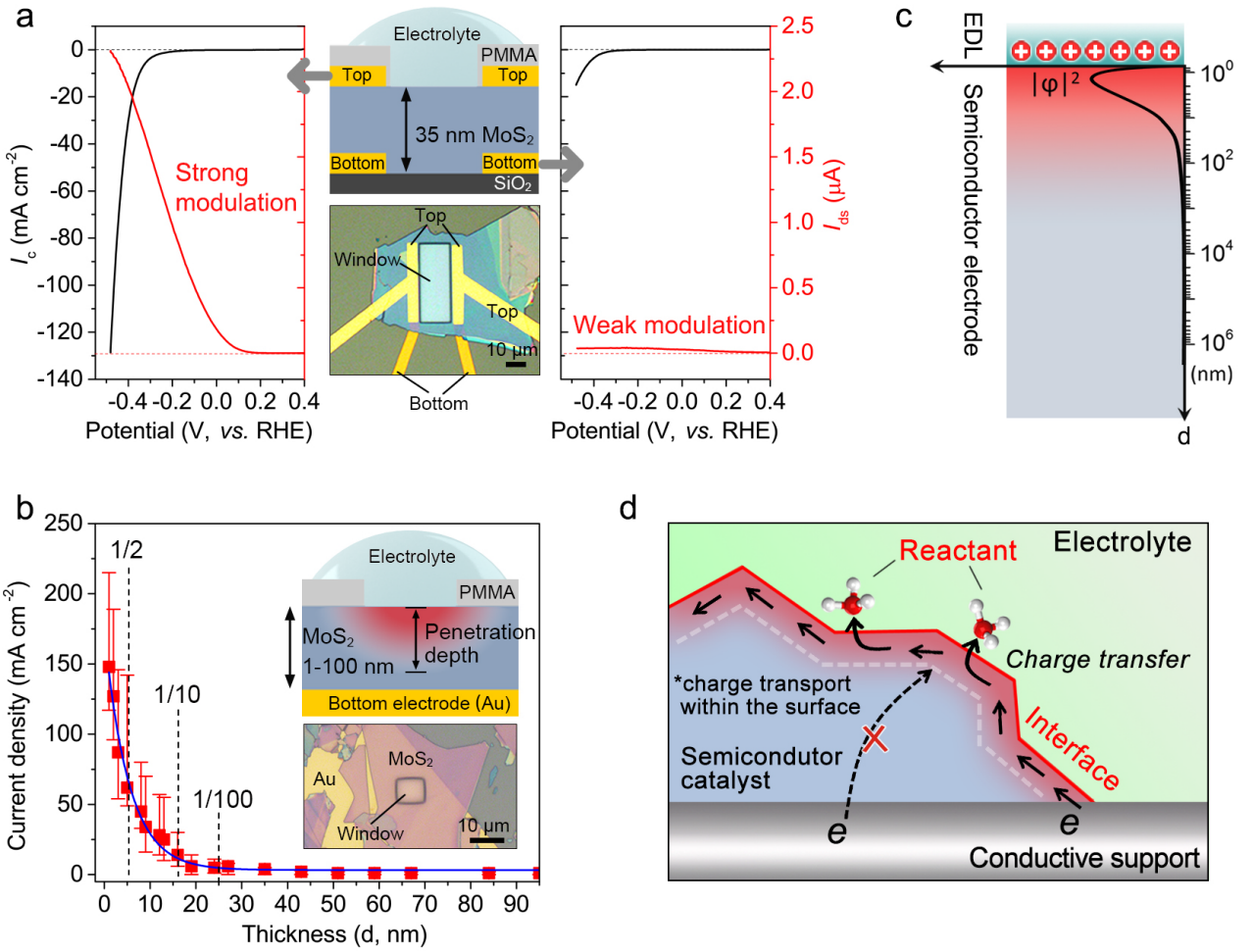

Figure 3. Self-gating modulated surface conductance of semiconductor catalyst. a, *In-situ* electronic/electrochemical measurements are performed on a 35-nm-thick MoS_2 flake in micro-cell with top (left curves) and bottom (right curves) electrodes. Middle panel: the schematic illustration of the micro-cell (top) and the corresponding optical microscopy image (bottom). **b,** HER activity (current density) of MoS_2 drops quickly with its thickness. Inset: the schematic illustration of micro-cell with bottom electrode (top) and the corresponding optical microscopy image (bottom). **c,** Calculated carrier density as a function of the thickness of semiconductor catalyst at the semiconductor-electrolyte interface under an electric field of the order of 10 MV cm^{-1}. A high carrier density is realized on the surface of semiconductor electrode. **d,** Schematic illustration of the surface conductance of semiconductor electrocatalyst. A surface conductive pathway is formed when the surface of the semiconductor electrocatalyst is turned on by the electrochemical potential under self-gating, allowing the charges transfer via the semiconductor-electrolyte interface, *i.e.*, the electrocatalytic reaction happens.

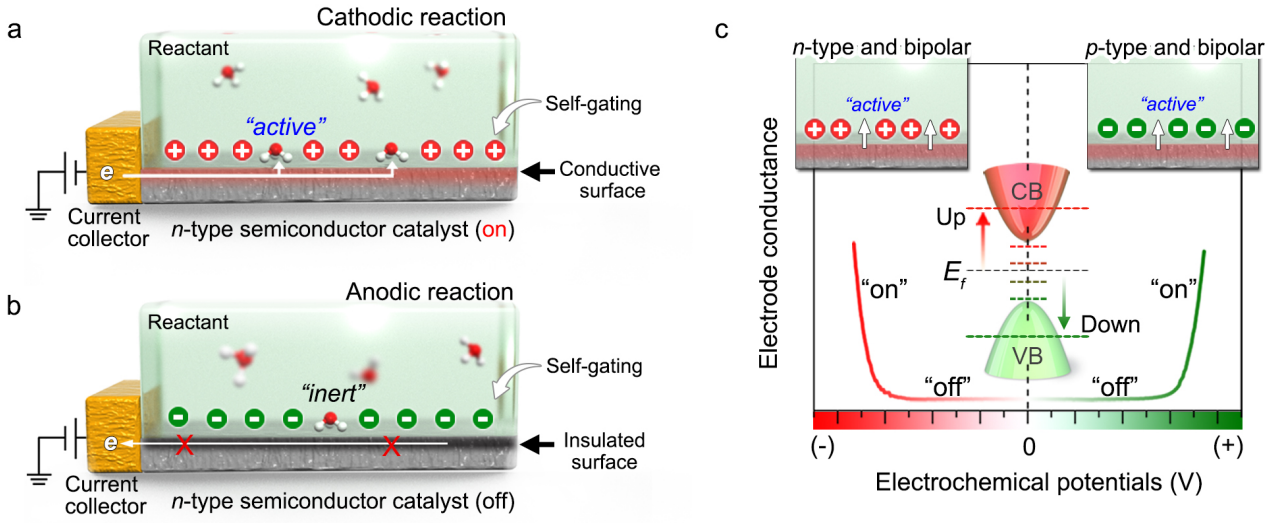

Figure 4. Correlation of the charge carrier type and the reaction in semiconductor catalyst. a-b, Schematic illustration of the effect of the surface conductance on *n*-type semiconductor catalyst for cathodic reaction (a) and anodic reaction (b). The self-gating turns on the surface of *n*-type semiconductor (surface conductive) in cathodic potential, facilitating the electron transport and making the surface "active" (a). On the contrary, its surface is turned "off" (surface insulated) at anodic potential under self-gating (b), making the surface "inert". **c,** Schematic illustration of the correlation between the types of the semiconductors and their preferred electrocatalytic activities. *n*-type and bipolar semiconductors can be turned on by the negative electrochemical potential, making them suitable for cathodic reactions. *p*-type and bipolar semiconductors can be turned on by the positive electrochemical potential, thus suitable for anodic reactions.

Table 1. Correlation between the charge carrier types of previously studied semiconductor catalysts and their preferred electrocatalytic reactions. The corresponding literatures are listed in Supplementary Table S4.

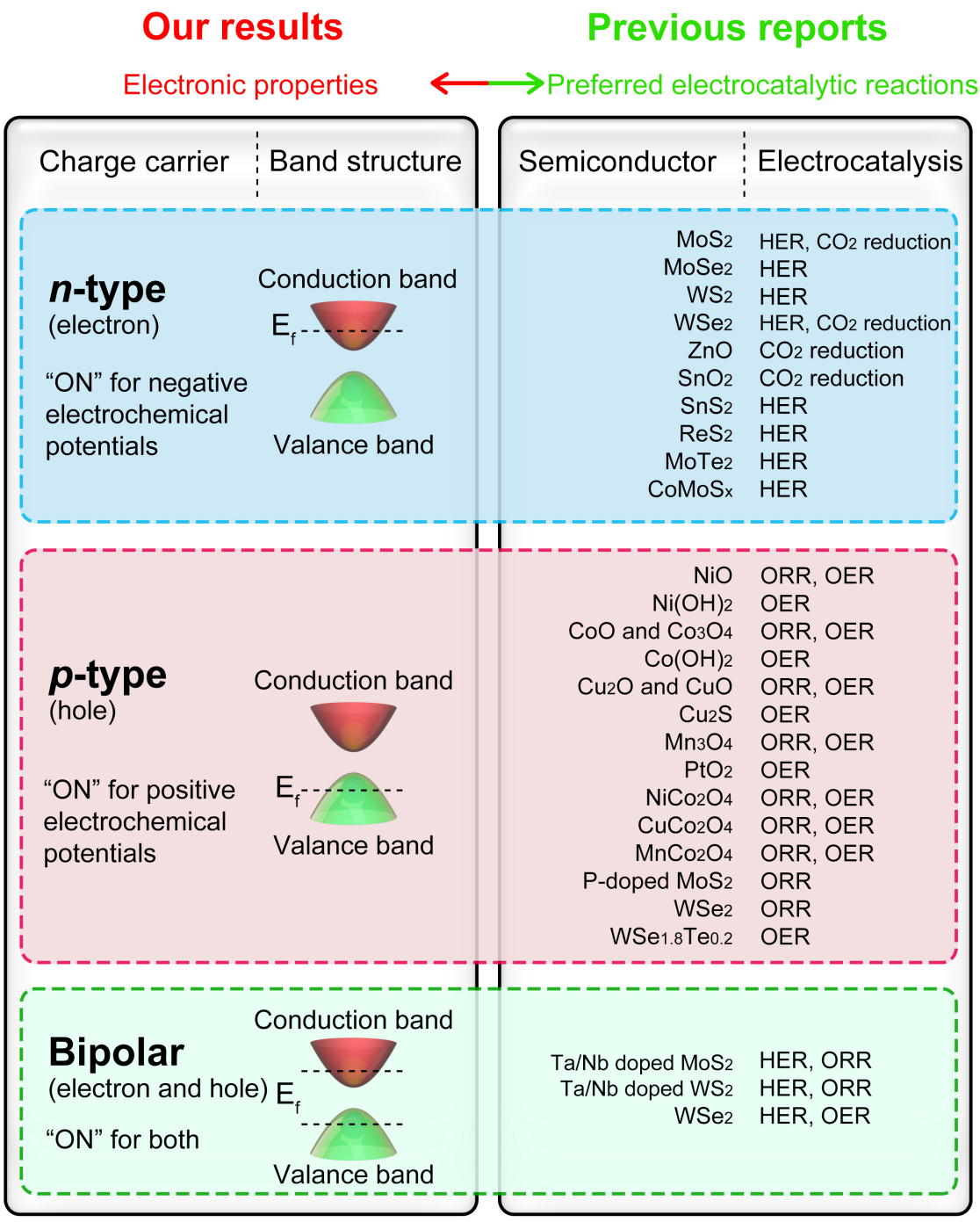

Note: some metallic group VIA compounds, such as metal chalcogenides (*e.g.* CoS_2, $CoSe_2$, NiS_2, $NiCo_2S_4$, VS_2, VTe_2, and $PtTe_2$) and metallic metal oxides (*e.g.* RuO_2, RhO_2, IrO_2, $PtCoO_2$, and $PdXO_2$ [X=Co, Cr, or Rh]) are not listed. Please see the detailed discussion in Supplementary Note 6.

References

1 Allen J. Bard, L. R. F. *Electrochemical Methods: Fundamentals and Applications-2nd Edition*. (Wiley-VCH, 2000).

2 Memming, R. *Semiconductor Electrochemistry-2nd Edition*. (Wiley-VCH, 2015).

3 Rajeshwar, K. *Fundamentals of Semiconductor Electrochemistry and Photoelectrochemistry*. Vol. 6 (Wiley-VCH, 2002).

4 Nozik, A. J. & Memming, R. Physical Chemistry of Semiconductor-Liquid Interfaces. *J. Phys. Chem.* **100**, 13061-13078 (1996).

5 Gao, Y. Q., Georgievskii, Y. & Marcus, R. A. On the theory of electron transfer reactions at semiconductor electrode/liquid interfaces. *J. Chem. Phys.* **112**, 3358-3369 (2000).

6 Lewis, N. S. Progress in Understanding Electron-Transfer Reactions at Semiconductor/Liquid Interfaces. *J. Phys. Chem. B* **102**, 4843-4855 (1998).

7 Fajardo, A. M. & Lewis, N. S. Rate Constants for Charge Transfer Across Semiconductor-Liquid Interfaces. *Science* **274**, 969-972 (1996).

8 Marcus, R. A. On the Theory of Oxidation-Reduction Reactions Involving Electron Transfer. I. *J. Chem. Phys.* **24**, 966-978 (1956).

9 Gerischer, H. Charge transfer processes at semiconductor-electrolyte interfaces in connection with problems of catalysis. *Surf. Sci.* **18**, 97-122 (1969).

10 Bisri, S. Z., Shimizu, S., Nakano, M. & Iwasa, Y. Endeavor of iontronics: from fundamentals to applications of ion-controlled electronics. *Adv. Mater.* **29**, 1607054 (2017).

11 Du, H., Lin, X., Xu, Z. & Chu, D. Electric double-layer transistors: a review of recent progress. *J. Mater. Sci.* **50**, 5641-5673 (2015).

12 Wang, Y. *et al.* Structural phase transition in monolayer $MoTe_2$ driven by electrostatic doping. *Nature* **550**, 487 (2017).

13 Saito, Y., Kasahara, Y., Ye, J., Iwasa, Y. & Nojima, T. Metallic ground state in an ion-gated two-dimensional superconductor. *Science* **350**, 409-413 (2015).

14 Vanmaekelbergh, D., Houtepen, A. J. & Kelly, J. J. Electrochemical gating: A method to tune and monitor the (opto)electronic properties of functional materials. *Electrochim. Acta* **53**, 1140-1149 (2007).

15 Saito, Y. *et al.* Superconductivity protected by spin-valley locking in ion-gated MoS_2. *Nat. Phys.* **12**, 144-149 (2016).

16 Ye, J. T. *et al.* Liquid-gated interface superconductivity on an atomically flat film. *Nat. Mater.* **9**, 125-128 (2010).

17 Liu, L. *et al.* Probing the Crystal Plane Effect of Co_3O_4 for Enhanced Electrocatalytic Performance toward Efficient Overall Water Splitting. *ACS Appl. Mater. Interfaces* **9**, 27736-27744 (2017).

18 Ling, T. *et al.* Engineering surface atomic structure of single-crystal cobalt (II) oxide nanorods for superior electrocatalysis. *Nat. Commun.* **7**, 12876 (2016).

19 Yu, Y. *et al.* High phase-purity 1T'-MoS_2- and 1T'-$MoSe_2$-layered crystals. *Nat. Chem.* **10**, 638-643 (2018).

20 Jaramillo, T. F. *et al.* Identification of active edge sites for electrochemical H_2 evolution from MoS_2 nanocatalysts. *Science* **317**, 100-102 (2007).

21 Li, H. *et al.* Activating and optimizing MoS_2 basal planes for hydrogen evolution through the

formation of strained sulphur vacancies. *Nat. Mater.* **15**, 48-53 (2016).
22 Voiry, D., Yang, J. & Chhowalla, M. Recent strategies for improving the catalytic activity of 2D TMD nanosheets toward the hydrogen evolution reaction. *Adv. Mater.* **28**, 6197-6206 (2016).
23 Franklin, A. D. *Electrocatalysis on Non-metallic Surfaces*. (National Bureau of Standards, 1975).
24 Ding, M. *et al.* An on-chip electrical transport spectroscopy approach for *in situ* monitoring electrochemical interfaces. *Nat. Commun.* **6**, 7867 (2015).
25 Ding, M. *et al.* Nanoelectronic investigation reveals the electrochemical basis of electrical conductivity in *shewanella* and *geobacter*. *ACS Nano* **10**, 9919-9926 (2016).
26 Zhang, Y. *et al.* Chemical vapor deposition of monolayer WS_2 nanosheets on Au foils toward direct application in hydrogen evolution. *Nano Res.* **8**, 2881-2890 (2015).
27 Fujimoto, T. & Awaga, K. Electric-double-layer field-effect transistors with ionic liquids. *Phys. Chem. Chem. Phys.* **15**, 8983-9006 (2013).
28 Chhowalla, M., Jena, D. & Zhang, H. Two-dimensional semiconductors for transistors. *Nat. Rev. Mater.* **1**, 16052 (2016).
29 DasA *et al.* Monitoring dopants by Raman scattering in an electrochemically top-gated graphene transistor. *Nat. Nanotechnol.* **3**, 210-215 (2008).
30 Braga, D., Gutiérrez Lezama, I., Berger, H. & Morpurgo, A. F. Quantitative determination of the band gap of WS_2 with ambipolar ionic liquid-gated transistors. *Nano Lett.* **12**, 5218-5223 (2012).
31 Ortiz, D. N. *et al.* Ambipolar transport in CVD grown $MoSe_2$ monolayer using an ionic liquid gel gate dielectric. *AIP Adv.* **8**, 035014 (2018).
32 Chen, X. *et al.* Probing the electron states and metal-insulator transition mechanisms in molybdenum disulphide vertical heterostructures. *Nat. Commun.* **6**, 6088 (2015).
33 Chu, L. *et al.* Charge transport in ion-gated mono-, bi-, and trilayer MoS_2 field effect transistors. *Sci. Rep.* **4**, 7293 (2014).
34 Xia, J., Chen, F., Li, J. & Tao, N. Measurement of the quantum capacitance of graphene. *Nat. Nanotechnol.* **4**, 505 (2009).
35 Lezama, I. G. *et al.* Single-crystal organic charge-transfer interfaces probed using Schottky-gated heterostructures. *Nat. Mater.* **11**, 788 (2012).
36 Toshihiko, K., Taishi, T., F., M. A. & Yoshihiro, I. Organic Single-Crystal Schottky Gate Transistors. *Adv. Mater.* **21**, 3689-3693 (2009).
37 Neamen, D. *Semiconductor Physics And Devices*. (McGraw-Hill, Inc., 2003).
38 Xu, Z. J. From Two-Phase to Three-Phase: The New Electrochemical Interface by Oxide Electrocatalysts. *Nano-Micro Letters* **10**, 8 (2017).
39 Suntivich, J., May, K. J., Gasteiger, H. A., Goodenough, J. B. & Shao-Horn, Y. A Perovskite Oxide Optimized for Oxygen Evolution Catalysis from Molecular Orbital Principles. *Science* **334**, 1383-1385 (2011).
40 Liang, Y. *et al.* Co_3O_4 nanocrystals on graphene as a synergistic catalyst for oxygen reduction reaction. *Nat. Mater.* **10**, 780 (2011).
41 Wei, C. *et al.* Cations in Octahedral Sites: A Descriptor for Oxygen Electrocatalysis on Transition-Metal Spinels. *Adv. Mater.* **29**, 1606800 (2017).
42 Liu, Y. *et al.* Self-optimizing, highly surface-active layered metal dichalcogenide catalysts for

hydrogen evolution. *Nat. Energy* **2**, 17127 (2017).
43 Burke, M. S., Kast, M. G., Trotochaud, L., Smith, A. M. & Boettcher, S. W. Cobalt-Iron (Oxy)hydroxide Oxygen Evolution Electrocatalysts: The Role of Structure and Composition on Activity, Stability, and Mechanism. *J. Am. Chem. Soc.* **137**, 3638-3648 (2015).
44 Trotochaud, L., Young, S. L., Ranney, J. K. & Boettcher, S. W. Nickel-Iron Oxyhydroxide Oxygen-Evolution Electrocatalysts: The Role of Intentional and Incidental Iron Incorporation. *J. Am. Chem. Soc.* **136**, 6744-6753 (2014).
45 Seh, Z. W. *et al.* Combining theory and experiment in electrocatalysis: insights into materials design. *Science* **355** (2017).

Acknowledgements

This work was supported by MOE under AcRF Tier 1 (M4011782.070 RG4/17 and M4011993.070 RG7/18), AcRF Tier 2 (2015-T2-2-007, 2016-T2-1-131, 2016-T2-2-153 and 2017-T2-2-136) and AcRF Tier 3 (2018-T3-1-002), and A*Star QTE programme. This work was also supported by MOE under AcRF Tier 2 (2015-T2-2-057, 2016-T2-2-103, 2017-T2-1-162) and AcRF Tier 1 (2016-T1-002-051, 2017-T1-001-150, 2017-T1-002-119), and NTU under Start-Up Grant (M4081296.070.500000) in Singapore. H.Z. thanks the support from ITC via Hong Kong Branch of National Precious Metals Material Engineering Research Center, and the Start-Up Grant from City University of Hong Kong. We would like to acknowledge the Facility for Analysis, Characterization, Testing and Simulation, Nanyang Technological University, Singapore, for use of their electron microscopy facilities. Q.J.W. acknowledges the support of the Ministry of Education- Singapore grant (MOE2016-T2-1-128) and National Research Foundation-Competitive Research Program (NRF-CRP18-2017-02). Z.W.S. acknowledges the support of the Institute of Materials Research and Engineering, A*STAR (IMRE/17-1R1211). We thank Zhichuan J. Xu for discussions about surface conductance. We thank Lijuan Han, Jose Ramon Galan-Mascaros (Institute of Chemical Research of Catalonia, Spain), and Pengyi Tang (Catalonia Institute for Energy Research, Spain) for discussions about EIS. We thank Yuan Liu (Hunan University, China) for discussions about semiconductor electronic device. We also thank Salim Teddy for XPS measurement and data analysis.

Author Contributions

H.Z. and Z.L. guided the project. Y.H. and Q.H. observed the self-gating phenomenon, designed the experiments, fabricated the devices and performed *in-situ* electronic/electrochemical and EIS measurement and analysis. Q.H., Y.H., M.D., C.Z., and S.G. made the micro-cell setup. L.W., Z.Z.,

and B.Y. performed the first-principle calculations, and analyzed the simulation data. Y.H., P.G., C.G., and X.W. synthesized single-layer TMD nanosheet. P.Y., Q.Z., F.L., L.W., and M.W. synthesized TMD crystals. X.Y. synthesized Si nanowires. Z.X., A.H., Z.S. analyzed the electrochemical results, and revised the manuscript. Y.H., Q.H., H.Z., and Z.L. conceived and supervised the experiments. Y.H., Q.H., Q.W., H.Z., and Z.L. wrote the paper. All authors discussed the results and commented on the manuscript.

Additional information

Supplementary information is available in the online version of the paper.

Reprints and permissions information is available online at www.nature.com/reprints.

Correspondence and requests for materials should be addressed to H.Z. or Z.L.

Publisher's note: Springer Nature remains neutral with regard to jurisdictional claims in published maps and institutional affiliations.

Competing financial interests

The authors declare no competing financial interests.

Methods

Growth of single-layer WS_2

Chemical vapor deposition (CVD) was employed to grow single-layer WS_2 with the halide-assisted atmospheric pressure growth.[46] The mixture of WO_3 and NaCl, referred to as WO_3/NaCl, and S powders used as precursors, were placed in the center and upstream of the tube furnace, respectively. Excess S is supplied such that the vapor is sufficient for large-area growth of WS_2. High-purity Ar was served as the carrier gas, and a clean SiO_2 (285 nm)/Si wafer was used as the growth substrate which was face-down on top of WO_3/NaCl (8:1 mass ratio). Before the growth process, the tube furnace was thoroughly purged with Ar (500 sccm) for 10 min to remove trace-amount air. The growth temperature was kept at 750–820 °C under 50 sccm Ar flow at the atmospheric pressure, while S powder was kept at approximately 160 °C. After the growth for 10-15 min, the furnace was naturally cooled down to room temperature.

Introduction of four types of micro-cells

There are four types of micro-cells developed in our work, as shown in Fig. S1, *i.e.*, Type 1: micro-cell for *in-situ* electronic/electrochemical measurement, which can simultaneously collect the electronic and electrochemical signals of semiconductor electrocatalysts at a large potential window; Type 2: micro-cell for thickness-dependent electrocatalytic measurement, which can examine the HER performance of MoS_2 with various thicknesses (1-101 nm) to obtain the penetration depth of the surface conductance (in this micro-cell, the electrochemical current transports vertically through the semiconductor to the bottom electrode); Type 3: micro-cell for top and bottom electrode measurement, which can investigate the surface and bulk conductance of the semiconductor flake; and Type 4: micro-cell for photoelectrochemical measurement, which

can measure not only the photo-conductance and photo-electrochemical current simultaneously, but also the photo-response time at various electrochemical potentials.

Fabrication of micro-cells for in-situ electronic/electrochemical measurement

The typical fabrication procedure is shown in Fig. S2. First, a 16 mm × 16 mm SiO_2 (285 nm)/Si chip with pre-patterned 32 Au contact pads was fabricated using the conventional photolithography. Then, the CVD-grown single-layer WS_2 (left panels in Fig. S2) or mechanically exfoliated TMDs (MoS_2, WSe_2, $WSe_{1.8}Te_{0.2}$,[47] $ReSe_2$, $PtSe_2$ and $MoTe_2$) nanosheets (right panels in Fig. S2) were transferred onto the chips. The mechanically exfoliated TMD nanosheets were treated by the Ar plasma (3 W at 6.5×10^{-3} Torr for 15 s) to create S, Se, or Te vacancies (2-4%) to provide more active sites[21]. After that, the e-beam lithography, followed by thermal or electron-beam evaporation, were used to fabricate metal contacts used for the drain and source, which contact the Au pads on the chip (metal contacts: Cr (5 nm)/Au (60 nm) for MoS_2, ReS_2, and single-layer WS_2; Pd (5 nm)/Au (60 nm) for $WSe_{1.8}Te_{0.2}$; Ti (5 nm)/Au (60 nm) for WSe_2, $PtSe_2$, and $MoTe_2$). Finally, the device chip was passivated with 1-μm-thick poly(methylmethacrylate) (PMMA) film, followed by the e-beam lithography process to open a window through PMMA to expose the region of interest on the nanosheet.

As a control experiment, Pt microelectrode was fabricated onto the chip by laser writing followed by electron-beam evaporation of 40 nm Pt. The following processes are similar to those used for fabrication of micro-cells.

Fabrication of micro-cells for top and bottom electrode measurement

The typical fabrication procedure of the micro-cell with top and bottom electrodes is shown in Fig. S21. Two bottom-electrodes (Cr/Au, 2 nm/15 nm) was first fabricated to contact the Au contact

pads by e-beam lithography followed by thermal evaporation. Second, MoS_2 nanosheet with thickness of 20-40 nm was mechanically exfoliated onto PDMS, and then dry transferred onto the targeted bottom electrode. Third, two top-electrodes (Ti/Au, 2 nm/80 nm) were fabricated on the MoS_2 nanosheet, which are vertically aligned to the bottom electrode (without direct contact) by e-beam lithography followed by thermal evaporation. Fourth, sulphur vacancies (≈ 10 %) were introduced in MoS_2 by the Ar plasma (3 W for 45 s at 6.5×10^{-3} Torr) to increase the active sites. The devices were then passivated with 1-μm-thick PMMA film, followed by e-beam lithography to open a reaction window on the basal plane of MoS_2 while avoiding the exposure of the edges and electrodes. Additionally, the devices with in-plane top and bottom electrodes (Fig. S21-4B) were also tested in our experiment, behaving similarly to the vertically aligned ones.

Fabrication of micro-cells for thickness-dependent electrocatalytic measurement

The typical fabrication procedure for the micro-cells with different thicknesses (1-100 nm) of MoS_2 nanosheets is shown in Fig. S22. Briefly, both CVD-grown single-layer MoS_2 and mechanically exfoliated multilayer MoS_2 nanosheets were transferred onto Au contacts on SiO_2/Si chips. Sulphur vacancies (≈ 10 %) were then introduced in MoS_2 by the Ar plasma (3 W, 45 s) to increase the active sites. Atomic force microscopy (AFM) was used to confirm the thickness of MoS_2 nanosheets. Finally, all devices were passivated with 1-μm-thick PMMA film, followed by e-beam lithography to open reaction windows on the basal planes of MoS_2.

Fabrication of Si nanowire based micro-cell devices

Si nanowires were fabricated through chemical etching of light-doped Si wafers[48] (doping concentration $\approx10^{13}$ e cm^{-3}). The as-fabricated Si nanowires could be easily removed from the wafer surface, resulting in a homogenous suspension in isopropyl alcohol through low power

sonication. Then, Si nanowires were dropped casting onto pre-patterned chips with Au contact pads, which showed broad distributions of diameters (50-300 nm) and lengths (10-20 μm). By using TEM, the porous structures were observed on the surface of Si nanowires. Their edge-rich characteristic may provide active sites for the electrocatalysis. The device fabrication procedure is similar to that for TMD micro-cells described in the Materials and Methods Section, except for a thicker metal electrode (Cr/Au, 5 nm/200 nm).

In-situ electronic/electrochemical measurement in micro-cells

Micro-cell is appropriately setup to study the surface charge injection[49] and charge transfer processes[50] in a more controlled manner. In our work, the *in-situ* electronic/electrochemical measurement was conducted in a droplet of 0.5 M H_2SO_4 electrolyte in a micro-cell.

There are four electrodes in the micro-cell. Two are connected to graphite and Ag/AgCl micro reference electrode (Harvard Apparatus), used as the counter and references, respectively. The other two electrodes are connected to the TMD nanosheet as drain and source contacts to collect their electronic signals in electrocatalysis. In all experiments, only the exposed region of nanosheet contributes to the electrocatalytic performance, and the rest of area in contact with electrolyte is passivated with PMMA. During the HER (-0.4 V *vs*. RHE), the H_2 micro-bubble was only observed on top of the exposed MoS_2 surface, indicating that the electrochemical reaction only occurs in the reaction window (Fig. S3). Before the electrocatalytic measurements on TMD nanosheets, the fabricated Pt microelectrode in the reaction window (Fig. S4a) was tested. The Pt microelectrode shows a Tafel slope of 37.2 mV dec^{-1} and onset potential less than 10 mV (Fig. S4b-c), consistent with the reported result[21], proving that our micro-cell setup is suitable for the electrocatalytic reaction.

Representative data on *n*-type MoS_2 and bipolar WSe_2 nanosheets are collected during the *in-situ* electronic/electrochemical measurement (Fig. S5). The scan rate of electrochemical potential is 5 mV/step, and the scan direction follows zero → cathodic (HER) → zero → anodic (OER) → zero. The electronic (I_{ds}) and electrochemical (I_c) signals were recorded simultaneously. Normally, I_{ds} is about 10-1000 times I_c in our experiment, which is dependent on the conductance of the semiconductor catalyst and the bias voltage (V_{ds}). The electrochemical current density was calculated by normalizing the current to the open area of PMMA on the TMD nanosheets. In this work, we express the electrochemical reference voltage with respect to RHE, *i.e.*,

$$E_{RHE} = E_{Ag/AgCl} + 0.219\ V$$

Electrochemical impedance spectroscopy (EIS) measurement in micro-cells

The EIS measurements were performed on the MoS_2 nanosheet and Au microelectrodes in the respective micro-cells at various electrochemical potentials, from -0.14 to -0.38 V (*vs*. RHE), during HER, by using an Autolab PGSTAT204 in the frequency range of 10^2-10^5 Hz with an amplitude of 10 mV. Data fitting was conducted on the basis of a Randles equivalent circuit model, employing constant phase element (Q element, CPE) by using the Nova 2.1.2 software. Since I_c is very low in the micro-electrochemical setup (in the order of 10^{-8}-10^{-7} A), no gas bubble was observed during the EIS measurements. For each MoS_2 nanosheet microelectrode, the *in-situ* electronic/electrochemical measurement was conducted on the same device in order to compare the charge transport resistance with the value extracted from EIS measurements.

Material characterizations

The TMDs were characterized by optical microscopy, atomic force microscopy (AFM, Bruker 8 AFM microscope system under ScanAsyst mode), scanning electron microscopy (SEM, FEI 4200), and Raman spectroscopy (WITec alpha300 R) performed with a 532 nm laser (with spot size about 500 nm in diameter) at room temperature. The *in-situ* electronic/electrochemical measurements were performed by combining two source meters (Keithley 2400 and 2450).

Data availability

The data that support the findings of this study are available from the corresponding author on reasonable request.

References

46 Li, S. *et al.* Halide-assisted atmospheric pressure growth of large WSe_2 and WS_2 monolayer crystals. *Appl. Mater. Today.* **1**, 60-66 (2015).

47 Huang, J.-H. *et al.* Large-Area 2D Layered $MoTe_2$ by Physical Vapor Deposition and Solid-Phase Crystallization in a Tellurium-Free Atmosphere. *Adv. Mater. Interfaces* **4**, 1700157 (2017).

48 Salvatierra Rodrigo, V. *et al.* Silicon Nanowires and Lithium Cobalt Oxide Nanowires in Graphene Nanoribbon Papers for Full Lithium Ion Battery. *Adv. Energy Mater.* **6**, 1600918 (2016).

49 Voiry, D. *et al.* The role of electronic coupling between substrate and 2D MoS_2 nanosheets in electrocatalytic production of hydrogen. *Nat. Mater.* **15**, 1003-1009 (2016).

50 Wang, J. *et al.* Field Effect Enhanced Hydrogen Evolution Reaction of MoS_2 Nanosheets. *Adv. Mater.* **29**, 1604464 (2017).